Molecular Imaging with Spectral CT Nanoprobes

Dipanjan Pan, Anne H. Schmieder, Angana SenPan, Xiaoxia Yang, Samuel A. Wickline, Ewald Roessl, Roland Proksa, Carsten O. Schirra, and Gregory M. Lanza

1   Spectral Computed Tomography Imaging Technology

Traditional computerized tomography (CT) exploits the attenuation of photons traversing through an imaged object and impinging on a sensitive detector (or film) to create images. CT systems typically employ scintillation-based detector arrays that produce light when individual photons are absorbed. On a pixel-by-pixel basis, the integrated intensity of signal detected by the photodiode corresponds to the overall loss of signal intensity due to the intervening object represented. Despite the broad energy distribution of photons emitted in an X-ray beam and the known energy dependence of photon attenuation, traditional integrating detector measurements eliminate all inherent spectral information that might be used to further characterize the imaged object.

The two predominant physical causes of X-ray attenuation effects are the photoelectric process and Compton scattering [1]. From these factors, which can be differentiated with two measurements at distinct photon energies, the concept of "dual-energy" CT evolved and is now implemented in clinical practice. Dual-energy CT systems can be realized in two different ways, source-based and detection-based spectral separation. Source-based dual-energy CT is achieved utilizing conventional detector principles under X-ray exposure of different tube voltages.

D. Pan
Department of Bioengineering, University of Illinois at Urbana, Urbana, IL, USA

A.H. Schmieder • A. SenPan • X. Yang • G.M. Lanza, M.D., Ph.D. (✉)
Division of Cardiology, Department of Medicine, Washington University School of Medicine, CORTEX Building, Suite 101, 4320 Forest Park Avenue, Saint Louis, MO 63108, USA
e-mail: greg.lanza@mac.com

S.A. Wickline • E. Roessl • R. Proksa
Philips Research Hamburg, Hamburg, Germany

C.O. Schirra
Philips Research Brazil, São Paulo, Brazil

The kVp-switching method acquires X-ray projections at alternating tube voltages in order to obtain spectrally resolved measurements [2–5]. Another clinically available solution is dual-source CT which mounts two "source-detector" pairs on a single gantry with each pair operating at a different tube voltage. Detection-based spectral CT uses a single X-ray tube and instead a stack of detector-layers of which each layer is sensitive to different photon-energies. This "dual-layer" approach allows one to acquire both spectral measurements on the same projection path simultaneously in a single rotation of the gantry [6–12].

Advancements of the dual-layer CT energy-integrated detector technology were further extended into the development of photon-counting detectors, leading to the next generation of CT instrumentation often referred to as spectral or multicolored CT [13–17]. Photon-counting detectors produce a digital measure of photon energy through pulse height analysis that eliminates electronic noise. Photon-counting detectors simultaneously discriminate the energy of counted photons by assigning measured pulses into energy bins based on preselected thresholds. In principle, a multiplicity of spectral determinations characterizing multiple tissues and contrast agents within each voxel from the same X-ray beam can be made.

Electrons for all elements of the periodic table are distributed into energy shells, with the K-shell electrons closest to the nucleus possessing the lowest energy. When photons are iso-energetic with a K-shell electron, the photon can be fully attenuated, deploying its energy to free an electron on the K-shell. This ionization causes a discontinuity in the photoelectric attenuation cross-section, and is characteristic for each individual element. Elements between iodine and bismuth on the periodic chart possess K-shell electron energies within typical photon energy bandwidth of clinical CT, and each could serve a K-edge contrast agent. In particular, gold, gadolinium, ytterbium, tantalum, or bismuth are among the metals with K-edges well inside the X-ray beam energy bandwidth and promise the highest signal-to-noise levels [18, 19]. Iodine, which is a stalwart X-ray contrast element for traditional CT, is on the lower edge of the bandwidth. While useful for small animal preclinical spectral CT imaging, the low K-edge energy signal detected will be significantly compromised by photon starvation and scattering occurring as the X-ray beam passes through patient torsos. Some new CT contrast agents are being developed with iodine alone or as part of a hybrid multimodality approach, however the present chapter is focused on K-edge agents incorporating nontraditional radiopaque elements.

2   Spectral CT Contrast Agents: Challenges

Spectral CT contrast agents must be designed with metals with suitable K-shell energy electrons in order to absorb photons emitted in the X-ray beam. However, another significant challenge in the development of CT and spectral CT probes is the requisite high concentrations of metal that must be present within a voxel for detectability. In comparison with nuclear imaging, ultrasound, and even MRI, CT contrast imaging is very insensitive. High dosages of heavy metals are required to elicit effective CT contrast inherently bringing patient long-term safety into consideration.

This is particularly relevant since CT contrast probes will likely be used in many patients to rule-out disease and in others to serial assess and guide clinical management. Proving long-term human safety following exposure to heavy metals will be challenging unless the metal component of CT contrast agents are essentially bioeliminated over a reasonable time frame. A "what goes in must come out" philosophy regarding heavy metals should be embraced in the development of these pharmaceuticals.

Because the human renal clearance threshold for nanoparticles or their breakdown products is around 6–8 nm, the use of poorly degradable solid particles in excess of this size could ultimately result in prolonged or even indefinite retention of such contrast agents internally [20]. While some metal particles, such as iron oxides used for MRI imaging, are known to be metabolized slowly with the iron reentering the iron metabolic pool, other solid oxide or sulfide crystalline particles are unlikely to be metabolized and bioeliminated adequately. Even gold, which was used as a colloidal suspension for various medical applications since ancient times and in the more recent past for rheumatoid arthritis, may not be as inert as anticipated [21]. Large and or frequent dosages of gold particles (>8 nm) may clear the body very slowly or not at all. Proving that this or similar situations with other elements is safe to regulatory agencies will be a translational challenge that the field must recognize.

Rodent models are often used to study the pharmacology and safety of drugs of all types, including nanomedicines. In man, rabbits, and larger mammals, solid nanoparticles 8–10 nm or greater are above the renal threshold for glomerular clearance and must be metabolized into smaller constituent parts for elimination through the bile, urine, or respiration. However, the clearance mechanism of nanoparticles in rodents differs markedly from man and larger mammals. Particles of 250 nm or greater can pass directly into the biliary system of rats and mice within a few minutes of intravenous injection. Bulte et al. illustrated this phenomenon by acquiring an MR cholangiogram using proton and fluorine MR imaging of paramagnetic perfluorocarbon nanoparticles in rats [22] (Fig. 1). This MRI demonstration corroborated experimental
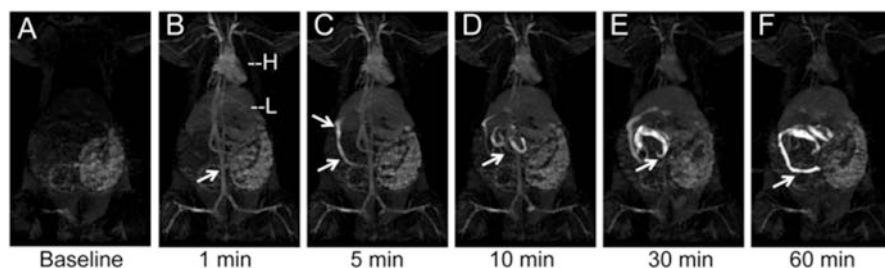

Fig. 1 3D time-of-flight (TOF) MR cholangiogram in a rat following intravenous injection of gadolinium-functionalized perfluorooctylbromide nanoparticles (NP). (**a**) Baseline image showing no evidence of vasculature or common bile duct. (**b**) 1 min post-injection, the blood pool as seen in the heart, aorta (*arrow*), and peripheral vasculature have strong T1-weighted positive contrast from the NP that are still constrained within the vasculature. *H* heart, *L* liver. (**c**) Within 5 min, the NP are rapidly excreted through the common bile duct (*arrows*), reflecting the rapid shunt of contrast from the liver into the small intestine. (**d**). After 10 min the small intestine contains most of the contrast, that is passed on to the large intestines at 30 min (**e**) and 60 min (**f**). Reproduced with permission from Ref. [22]

investigations of particle elimination dating to the 1950s and possibly decades earlier. In 1958, Hampton showed that intravenous particles in rodents distributed into Kupffer cells, hepatic cells, and bile within the liver [23]. This report cited and confirmed earlier reports of Müllendorf in 1916 and Weatherford in 1956 (*cited in* [23]) using colloidal dyes and India ink, respectively. Hampton demonstrated that particles phagocytosed by Kupffer cells were retained indefinitely; whereas, particles endocytosed by hepatocytes were transported rapidly into the biliary system, as imaged by Bulte. Interestingly, Hampton performed retrograde biliary infusions of Thorotrast™ colloidal particles and used transmission electron microscopy (TEM) to reveal that those particles transited in reverse through hepatocytes and into the space of Disse. While some of the Thoratrast™ became sequestered in Kupffer cells, much of it passed into the circulatory system. Similar evidence of nanoparticle excretion into rodent bile and feces include silica particles from 50 to 200 nm [24] citrate-coated silver particles (~8 nm) [25], and iron oxide core high-density lipoproteins (~10 nm) [26]. In larger non-rodent mammals, Juhlin [27] reported a few years later that fluorescent spherical hydrophilic particles of methyl methacrylate injected intravenously in rabbits did not transit effectively into the bile. Particles in the 20–110 nm produced very minimal biliary concentrations and those greater than 60 nm were not excreted into the biliary tree. While rodent models offer a wealth of research opportunity, species difference in biliary nanoparticle excretion must be considered to avoid incorrect conclusions regarding nanoparticle pharmacokinetics, pharmacodynamics, metabolism, bioelimination, and ultimately safety.

3   Spectral CT Contrast Agents

Many CT contrast agents have been created using metals with K-edge values within the X-ray energy bandwidth and the vast majority have crystalline cores that exceed 10 nm. While ultimately these types of agents may prove safe and effective, the scope of the present review generally considered small crystalline nanoparticles (<10 nm) and large degradable nanoparticles encapsulating small molecule organometallic complexes or small solid nanoparticles (<10 nm).

From a spectral CT perspective, two independent blood pool contrast agents imaged simultaneously may have important medical utility; however, the use of a single blood pool agent will likely have limited differential benefit over current iodine based approaches. For new contrast technologies to gain clinical and economic traction, they must address important unmet functional or biochemical (i.e., molecular) imaging needs. In some situations, this may be achieved through in situ labeling of cells, e.g., macrophages in inflammatory imaging, and in other situations by ligand-directed targeting. Regardless, the development of a molecular imaging agent should begin with a clear understanding of the unmet need, which then defines parameters for pharmaceutical design.

4   Bismuth

4.1   *Organobismuth Nanocolloid (NanoK)*

Emergency departments in the USA assess more than 8 million patients annually with complaints of chest pain or shortness of breath [28]. While a presumptive diagnosis of life-threatening acute coronary syndrome (ACS) may be apparent from the patient's initial presentation, the vast majorities of cases are equivocal and require the potential of cardiac involvement to be excluded. Consequently, individuals are retained for close observation and testing. For patient without cardiovascular symptoms, there is inconvenience, family stress, and high healthcare cost. Patients admitted for possible ACS require continuous cardiac telemetry, serial ECGs, and repeated cardiac troponin assays over 12–24 h. If cardiac infarction and unstable angina are excluded, then noninvasive cardiac stress testing is typically performed.

Coronary CT angiography has become increasingly refined and offers the potential to recognize patients with low likelihood of disease but the negative and positive predictive values do not meet the standard set by cardiac catheterization [29]. Moreover, coronary calcium, due to its attenuating and blooming artifacts, further complicates the clarity of the angiogram in the region of potentially critical disease [30]. Spectral CT contrast imaging offers an opportunity to target and detect intraluminal thrombus associated with acutely ruptured plaque while discriminating between attenuation artifacts of calcium deposits, which have low (K-edge energies (4.4 keV) (Fig. 2).

An initial approach to this medical imaging problem was reported by Pan et al. [31] using nanocolloids comprised of high concentrations of an organobismuth compound, bismuth neodecanoate, commixed in sorbitan sesquioleate. The phospholipid-encapsulated "soft" nanocolloid was 20 % w/v aqueous suspension with hydrodynamic diameters between 180 and 250 nm, a negative electrophoretic potential ranging from −20 to −27 mV, and 1.06 g/ml. The particle core was 12–14 wt% bismuth. The biocompatible outer lipid membrane can be functionalized for ligand-direct (peptide and antibody) homing to microthrombus (Fig. 3).

In vitro studies with the bismuth nanocolloid compared cross-sectional CT (conventional) and spectral CT images of phantoms containing serially diluted bismuth particles and a reference calcium acetate suspension in water. This illustrated the potential of K-edge imaging to segment calcium from bismuth nanocolloid despite the X-ray attenuation similarity of the materials at 60 keV, (Ca: 1060HU, Bi: 1050HU). As expected the attenuation of the bismuth formulation varied linearly with the element concentration ($R^2 = 0.999$).

Additionally, fibrin-targeted bismuth nanocolloid revealed excellent delineation and signal enhancement on spectral CT images of fibrin clot phantoms embedded with calcium. The control clot treated with targeted nonmetallic nanoparticles had negligible contrast, exhibiting only the highly attenuating calcium. The specific targeting of rhodamine-labeled bismuth particles to fibrin on human carotid endarterectomy specimens was corroborated microscopically with immunohistochemistry
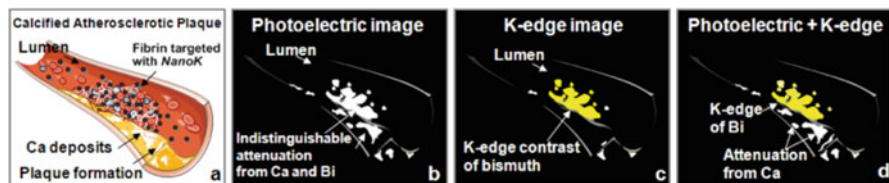
Fig. 2 Example of spectral CT using a coronary vascular example to illustrate the discrimination of calcium and spectral CT contrast agents; (**a**) coronary artery with a partial occluding thrombus emerging from rupture of the unstable intimal cap. (**b**) fibrin targeted with bismuth nanocolloid (BiNC) with in classic CT (photoelectric) image and attenuation due to calcium are seen (**c**) spectral CT (K-edge image) discriminates the fibrin-targeted BiNC from the calcium deposits, (**d**) integration of the classic CT X-ray image with the spectral CT molecular imaging result acquired simultaneously, reveals the signal from the fibrin-bound bismuth resolved from the atherosclerotic calcium deposits. Reproduced with permission from Ref. [31]

[31] and exemplified how the K-edge agent targeting was constrained to intravascular rather than intramural fibrin deposits. Dynamic imaging of NanoK with a clinical multidetector CT revealed that blood pool background was no longer detectable after 15–30 min, which would permit optimal molecular imaging of intraluminal thrombus after 1–2 h. The antibody-targeted fibrin bismuth agent concentrated in situ over the acute thrombus in 30 min, remained bound to the clot during 90 min continuous blood circulation, and was detected with a first generation spectral CT scanner as a partial-occlusive thrombus within a 1.41 mm diameter artery, equivalent to a small coronary artery in humans. The bismuth-enhanced clot was clearly differentiated within the vessel and distinct from adjacent attenuation effects of the femur. Superimposition of the simultaneously acquired K-edge image with the traditional CT image spatially oriented and localized the intravascular lesion relative to the rabbit's skeletal anatomy and demonstrated the complementarity of spectral CT molecular imaging and traditional CT [31] (Fig. 4).

Importantly, whole-body bioelimination of bismuth following intravenous injection was studied in adult male BALB/c mice in a 2-week pilot study. Nearly all of the metal was cleared from the mice within 14 days, and most was bioeliminated by the first week. The residual biodistribution on day 14 into primary particle clearance organs (i.e., liver, spleen, kidney) was assessed using inductively coupled plasma optical emission spectrometry in a second cohort of mice ($n=3$), which revealed less than 10 ppb (i.e., the lower detection limit). A third cohort of mice assessed the in vivo impact of bismuth nanocolloid and saline on liver (ALT, AST, albumin) and renal (BUN, CR, Na, K, Cl) function was assessed on days 1, 7, and 14 postinjection. All tests in both groups remained within accepted normal limits for each parameter and no statistical differences between groups were noted at any time point. The overarching conclusions from this early work were: (1) that the nanocolloid offered stable, detectable bismuth contrast for imaging, (2) that the organobismuth complexes could be bioeliminated, and (3) that the nanosystem acute toxicology was favorable [31].
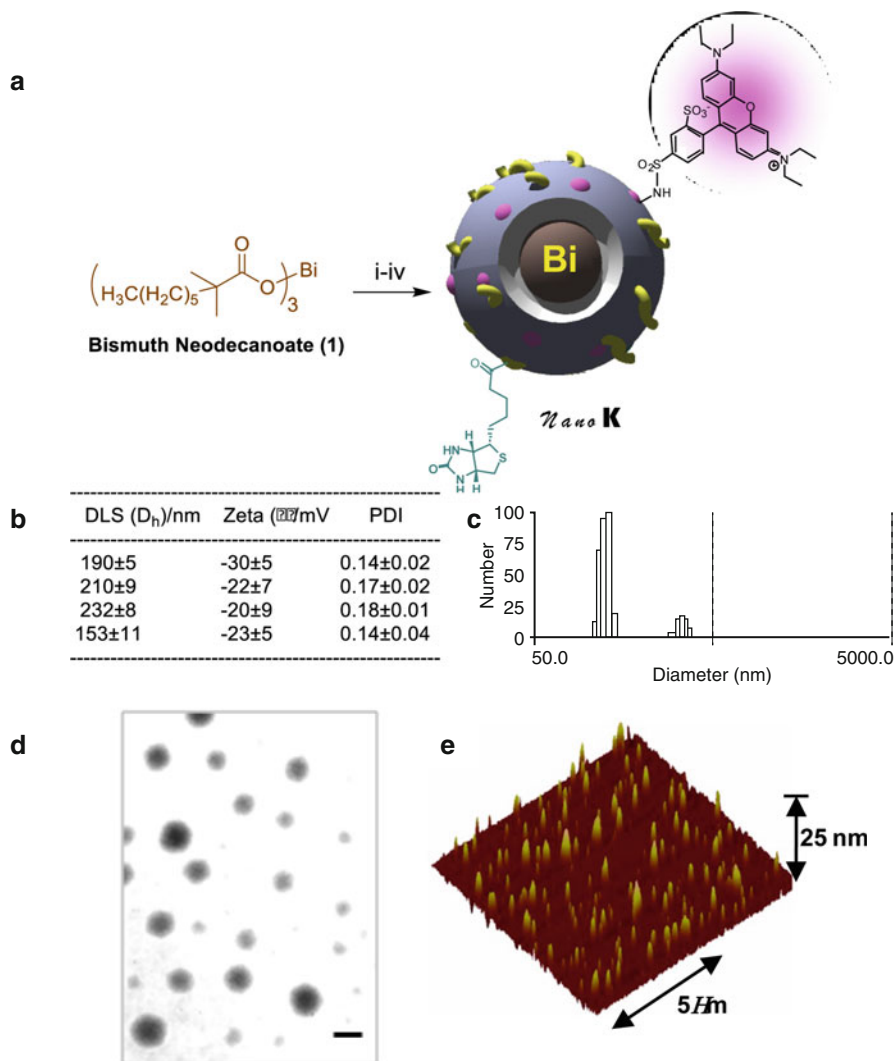
a

$$\left(H_3C(H_2C)_5 \underset{O}{\overset{O}{\|}} O\right)_3 Bi$$

Bismuth Neodecanoate (1)

i-iv →

Bi

$\mathcal{N}_{ano}$ **K**

b

DLS (D$_h$)/nm	Zeta (mV)	PDI
190±5	-30±5	0.14±0.02
210±9	-22±7	0.17±0.02
232±8	-20±9	0.18±0.01
153±11	-23±5	0.14±0.04

c

d

e

25 nm

5 μm

Fig. 3 Synthesis and physicochemical characterization of NanoK: (**a**) Schematic describing the preparation of bismuth-enriched K-edge nanocolloid (NanoK (Bi)): (**b**) characterization table for three replicates of NanoK; (**c**) hydrodynamic particle size distribution from dynamic light scattering (DLS); (**d**) anhydrous state TEM images (staining: uranyl acetate; scale bar: 100 nm; (**e**) Atomic force microscopy image (deposited on glass substrate). Reproduced with permission from Ref. [31]

4.2 Bismuth Sulfate: Alginate Microcapsules

The concept and benefit of small molecule bismuth contrast entrapped within larger particles or microcapsules was instituted by Barnett et al. [32]. These investigators addressed the challenge of pancreatic islet cells transplantation by entrapping the
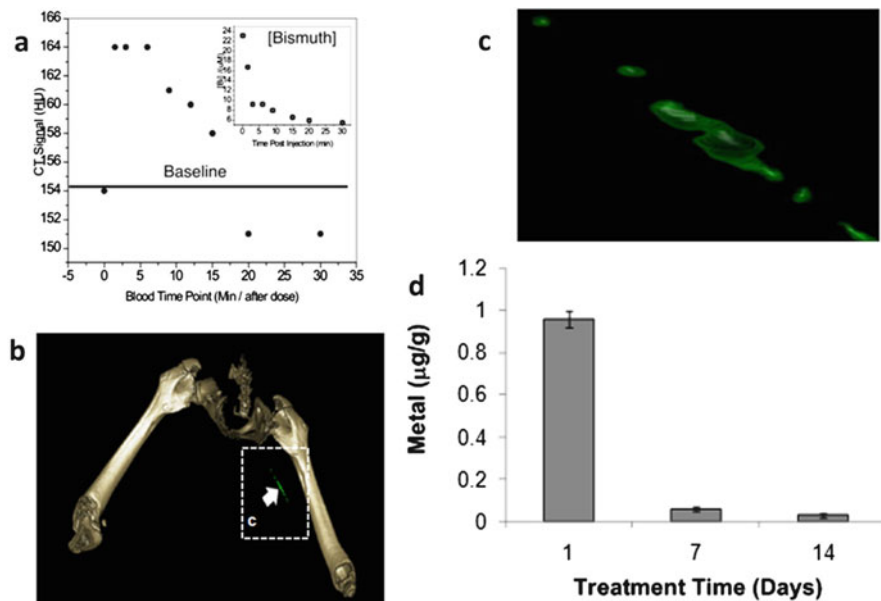
Fig. 4 (**a**) CT blood pool signal in rabbits following IV injection of NanoK. Inset shows the concentration of bismuth (ICP) in blood versus time post injection. Note that the background signal is at baseline in less than 30 min; (**b**, **c**) targeting in situ clot (thrombus) in rabbits (*arrow* indicates thrombus); (Scale: maximum clot diameter = 1.41 mm; minimum diameter = 1.25 mm). (**d**) Two weeks clearance profile of bismuth from mice. Reproduced with permission from Ref. [31]

cells and within a permeability selective bismuth-alginate capsule. The semipermeable capsule accommodated the influx of glucose and the responsive efflux of insulin, while excluding the penetration of humoral and cell-mediated immune factors. In this context, the bismuth-doped alginate offers radiopaque contrast to both guide implantation as well as support longitudinal monitoring capsule persistence. Upon the eventual metabolism of the capsule, the alginate and bismuth are metabolized or eliminated via urinary excretion. Traditional CT imaging provided very good spatial localization of the implants, however, spectral CT could provide quantitative estimates of bismuth content. Estimates of bismuth content can be converted into more precise assessment of microcapsule numbers and at least qualitative projections of islet numbers the adequacy of their insulin response to glucose challenge. Functional longitudinal monitoring afforded by quantitative spectral CT would clearly facilitate improved clinical management of these pancreatic surrogates.

4.3 Bismuth Sulfide Nanodots

Large-scale synthesis of bismuth sulfide (Bi_2S_3) nanodots was reported by Lu [33]. In contradistinction to the report from the Weissleder lab [34] using large crystalline bismuth particles, these nanodots had uniform particle sizes approximately 2–3 nm,

well below the renal clearance threshold. Although current production methods at that time for hydrophobic Bi_2S_3 nanoparticles lacked effective surface modification methods, Ai et al. coated the nanodots with either poly (vinylpyrrolidone) (PVP) for stability and biocompatibility. PVP-bismuth nanodots were compared in vivo to Iobitridol™, an X-ray contrast molecule with 45.6 wt% iodine. The intravenously administered nanodots circulated for 1 h and accumulated rapidly in the liver and spleen. Little bismuth was observed clearing via the kidneys into the bladder. Since these tiny particles were quickly sequestered into the mononuclear phagocyte system (MPS), one might infer that they aggregated in circulation. Subsequent histology showed no gross changes to clearance organ microanatomy, which is consistent with the expected low toxicity of nonionized bismuth. The Iobitridol™ control produced a very brief blood pool contrast then cleared through the kidney into the urine within 3 min. While prolonged blood pool contrast can be beneficial, particularly for techiques like MRI, a typical clinical CT imaging sequence is concluded in seconds, diminishing this advantage.

4.4 Dendrimeric Bismuth Sulfide

An alternative approach to coated minute bismuth nanoparticles was offered by the Shi laboratory, which reported the development of dendrimer-bismuth sulfide [35]. The agent was produced by reacting Bi^{3+} with generation 4 poly(amidoamine) dendrimers (G4.NGlyOH) followed by exposure to hydrogen sulfide to generate dendrimer coated-Bi_2S_3 nanoparticles, sized 5.2–5.7 nm. As expected, the X-ray contrast of dendrimer-bismuth sulfide was greater than that of iodine on an equimolar metal basis. The complex had minimal cellular cytotoxicity and good hemocompatibility. When injected subcutaneously in a rabbit thigh, the localized complex was readily appreciated with CT. However, when administered systemically in mice, the enhancement seen within the pulmonary vein and aorta was only slightly greater than an equimolar dosage of Omnipaque™, a commercially available iodine contrast agent. No pharmacokinetic, biodistribution, and bioelimination data of the dendrimer-bismuth sulfide were provided.

5 Gold

Gold nanoparticles and nanoshells have been extensively studied as optical, photoacoustic, and more recently X-ray contrast agents. Indeed the use of gold for optical contrast, particularly photoacoustic contrast agents, precedes later reports of its use for CT contrast nanoparticles, although it is long known to be X-ray attenuating. Many of the gold-based agents used for photoacoustic imaging are relatively large and exceed the renal threshold for clearance, but some are comprised of small gold nanoparticles alone or encased in larger nanoparticles.

5.1 Gold Nanobeacons

One important indication for nanotechnology has been the need for image-guided sentinel lymph node biopsy (SLNB) in patients with breast cancer and melanoma to stage metastases and avoid more invasive biopsy. Invasive SLNB can lead to seroma formation, lymphedema, sensory nerve injury, and limitation in the range of motion. Alternative noninvasive methods to identify sentinel lymph nodes (SLNs) in conjunction with either minimally invasive percutaneous fine-needle biopsy or molecular techniques could offer new prospects for noninvasive axillary staging of breast cancer. Pan et al. demonstrated the use of gold nanobeacons with varying gold nanoparticle content in the context of photoacoustic imaging; these gold nanobeacons were demonstrated to be highly effective for the same application with spectral CT [36–38]. The initial gold nanobeacons were designed as the encapsulation of octanethiol coated metallic gold nanoparticles (2–4 nm) suspended in vegetable and encapsulated with phospholipid with a nominal hydrodynamic diameter of 154 ± 10 nm. The polydispersity and zeta potential were measured to be 0.08 ± 0.03 and -47 ± 7 mV, respectively. Gold content, as determined by inductively coupled emission mass spectrometry, was 1080 μg/g of the 20 % colloid suspension (of GNB_{160}). For SLN mapping, GNB_{160} was compared with a polymer-encapsulated gold nanobeacons (GNB_{290}) developed through the self-assembly of amphiphilic di-block copolymer in aqueous media to entrap high payloads of gold. The same octanethiol coated AuNPs (2 w/v%) were suspended in polysorbate and microfluidized with a PS-*b*-PAA dispersion to obtain the GNB_{290} particles (particle size: 289 ± 24 nm, polydispersity index: 0.15 ± 0.04, gold: 134 μg/g or ~71,493 gold atoms per nanobeacon. While the original GNB was effective for SLN imaging, GNB_{290} was not due to its weight, inhibiting uptake and migration through the lymphatics following intradermal injection into the forepaw. Consequently, a smaller lipid-encapsulated (~90 nm) gold nanobeacon (GNB_{90}) was produced by suspending octanethiol-functionalized, coated AuNPs (2 w/v% of inner matrix) in polysorbate then microfluidizing the mixture with phospholipid-based surfactant. The GNB_{90} particle size was 92 ± 12 nm with a polydispersity of 0.35 ± 0.05. The gold content was only 1.56 μg/g or approximately 9 gold metal atoms per GNB_{90}. This particle and smaller payload rapidly transited from the forepaw intradermal injection site through the lymphatics into the SLN within a few minutes. The extent of lymph node uptake of the GNB_{90} particle far exceeded the original signal appreciated with GNB_{160} nanocolloid. For SLN imaging, it was evident that smaller particles with less gold/particle yielded more PA signal.

SLN mapping using GNB_{90} was next evaluated with spectral CT using an analogous experiment. As shown, the magnitude of the spectral CT image was dramatic, reflecting the high mass of gold accumulated rapidly into the node. The "soft" nature of the colloid, the incorporation of very small gold particles, and the very limited gold dose required for SLN imaging all contributed to what could be a translatable safe and effective formulation for this application [39] (Fig. 5).
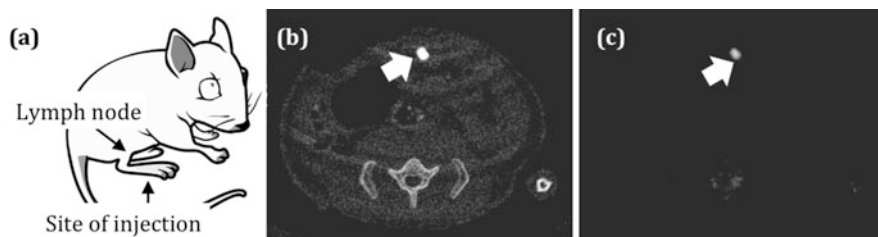
Fig. 5 In vivo noninvasive spectral CT imaging of SLN. (**a**) A cartoon illustrating the site of injection and the area of interest. 150 ml of nanobeacons were injected intradermally. (**b**) regional SLN were clearly contrasted on conventional CT. (**c**) K-edge contrast of accumulated gold nanoparticles in the SLN was selectively imaged with spectral CT. Reproduced with permission from Ref. [39]

5.2 High-Density Lipoprotein Gold Nanoparticles

The quest for distinguishing vulnerable versus stable atherosclerotic plaque prior to rupture remains a daunting challenge and unmet need in cardiovascular medicine. Since the early work of Benson [40] and Constantinides [41], the acute formation of thrombus following atherosclerotic plaque rupture has been well recognized as the etiology of unstable angina, myocardial infarction, transient ischemic attacks and stroke [42, 43]. Sensitive detection and differentiation of vulnerable versus stable atherosclerotic plaques in vessels with mild severity stenoses remains limited. As the PROSPECT trial showed, the current best invasive imaging technologies, i.e., angiograms and intravascular ultrasound, predict future regions of plaque rupture poorly, even in high-risk patients presenting with myocardial infarction [44]. While still inadequately understood, the risk of plaque rupture is primarily related to the composition of plaque, and considerable noninvasive imaging effort has been directed to characterizing the atherosclerotic inflammatory component.

In this regard, Cormode et al. developed a gold-enriched HDL nanoparticle mimetic as a relatively specific approach to labeling and identifying macrophage-rich plaques in the aortas of apoprotein E knock-out mice (APO$^{e-/e-}$) using micro-CT [45]. As previously discussed plaque is often laden with calcium deposits, which like gold has marked X-ray attenuation that can be differentiated with spectral CT. Moreover, spectral CT was employed to differentiate the uptake of the gold HDL particles in APO$^{e-/e-}$ mice from the iodine contrast enhancement of the aortic lumen [46, 47]. Although these first-generation photon-counting scanners had very slow image acquisition speeds unable to support live animal studies, this seminal report offered the first in vivo illustration of multi-spectral imaging potential in a pathological animal model. Moreover, in contradistinction to earlier versions of this gold-HDL approach, the nanosystem used in this study incorporated gold particles

of 3 nm with the overall diameter of the HDL particle around 7 nm, basically one gold particle per HDL particle. The dose of gold used was around 500 mg/kg, somewhat higher than a typical iodine contrast load (370 mg/kg). Given the small size of the gold particles, they have the potential for renal clearance, but given the dosage of particles required for in situ macrophage labeling, the long-term bioelimination of the metal will need to be better characterized.

5.3 *Pegylated Dendrimer Entrapped Gold Nanoparticles*

Peng and Shi [48] recently reported on the development of a polyethylene glycol (PEG)ylated dendrimer containing gold nanoparticles as a vehicle to achieve prolonged blood pool circulation. Indeed, prolonged blood pool contrast, particularly if it is vascular constrained has merit, but one must also be cognizant that the speed of photon-counting is already approaching clinical CT acquisition rates and current rapid imaging of approved iodinated agents with CT presents a high barrier to overcome. Peng and Shi synthesized and characterized amine-terminated poly(amidoamine) dendrimers (generation 5) that were partially modified by PEG monomethylether and gold salt. The dendrimers were 2–4 nm, had low acute toxicity up to 100 μM, and offered a circulatory half-life between 31 and 42 h depending on the gold density. Subsequently, Shi et al. reported the tripeptide arginylglycylaspartic acid (RGD) functionalization of this dendrimeric-gold construct and demonstrated its binding and potential X-ray benefits in vitro [49]. Clearly, this recent work is still evolving and seeks to take advantage of the metal concentration benefits accrued by targeting to increase imaging detectability of occult pathologies.

5.4 *Gold-Loaded Polymeric Micelles*

The Tsourkas lab [50] followed an approach similar to that described by Pan et al. in development of the polymer-encapsulated gold nanobeacons (GNB_{290}) [37]. These investigators took advantage of the higher X-ray attenuation properties of gold versus iodine and constructed PEG-b-poly(e-caprolactone) particles between 25 nm and 150 nm that entrapped 1.9 nm gold particles to augment CT-guided radiation therapy and radiosensitization. Radiosensitization of gold stems primarily from photoelectrons generated in the kilovolt energy range and theoretically from Auger electrons within the megavolt realm [51]. Radiation therapy in the presence of gold particles increases the extent of DNA fragmentation and treatment efficacy [52, 53]. This therapeutic response was corroborated with a 75 nm version of this nanotechnology.

Similar to the gold dendrimers described above, these polymeric gold particles had extended circulatory half-lives with enhanced blood pool contrast extending for 24 h. The particles were passively entrapped within the tumor periphery, as has been

described before for most nanoparticles. In combination with radiation therapy median survival of tumor-bearing mice was increased by 1.7-fold. Issues of acute toxicity and clinical pathology changes in mice receiving the nanoparticles were unremarkable. Issue of inflammation and biocompatibility associated with the "suture-like" polymer, the bioelimination of gold, and other long-term safety concerns will need to be further elucidated. Once again, this technology points to contrast designs that avoid large solid particle bioelimination issues by encapsulating numerous small particles with potentially filterable into the urine.

6   Tantalum Oxide

Other metals within the X-ray bandwidth include tantalum, which is chemically inert and offers good radiopacity. Although the metal oxide is water insoluble, Bonitatibus et al. [54] developed a coated water-soluble version 6 nm particle size. While the desirable X-ray properties of tantalum have been known, these investigators provide the first work to permit the nanocrystal to be suitable for intravenous injection at high concentration without aggregation. The tantalum oxide core was coated with (2-diethylphosphato-ethyl)triethoxysilane to form a homogeneous product concept stable at least for 6 months. Tantalum had greater X-ray attenuation versus iodine across the X-ray spectrum, particularly for the higher peak kilovoltages (kVp) in which realm the augmenting K-edge benefit that iodine enjoys with typical CT X-ray beams is missing. Using dynamic contrast imaging over 30 s, the higher and more persistent attenuation achieved with the tantalum oxide was appreciated versus iodine. Although the difference in contrast between the metals at baseline was modest, the rapid loss of iodinated contrast from the blood pool over 30 s led to progressively less iodine contrast relative to the more slowly clearing tantalum particles. This proof of concept study demonstrated yet another potential translatable approach to CT and K-edge imaging. Metal bioelimination, safety, and optimized efficacy for a specific unmet clinical are pending.

Along a similar line of investigation, the Hyeon and Choi laboratories [55] reported a silane modified PEG-coated tantalum oxide nanoparticle that was further functionalized with a fluorescent dye and applied to SLN mapping and blood pool imaging. The low end of the nanocrystal particle size distribution by TEM was 6 nm while the other particles had greater size reaching 15 nm with hydrodynamic particle size averaging just under 20 nm. For blood pool imaging, high dose (840 mg/kg) of the tantalum produced strong blood pool contrast with MPS clearance into the liver and spleen. For SLN mapping, the enhanced CT contrast obtained was corroborated with optical imaging for the bimodal agent. No acute safety problems were reported, but the issues of metal bioelimination, safety, and specific clinical application remain to be elucidated, particularly for the larger particle population.

7   Ytterbium

Ytterbium (Yb) based nanomaterials are particularly interesting from a K-edge imaging perspective. Yb has a K-edge at 61 keV, which is in the middle of the higher energy X-ray spectrum used clinically. At this spectral location the flux of photons impinging on the detector at somewhat higher and lower energies affords better resolution of the K-edge discontinuity than that observed on either extreme end of the bandwidth. Ytterbium is a lanthanide metal that is highly abundant at much lower cost than other relevant metals, particularly gold. However, as a lanthanide similar to gadolinium, unsuspected safety issues, including the potential for nephrogenic systemic fibrosis, will need to be carefully assessed.

The Lu laboratory [56] reported a Yb-based nanoparticulate that had prolonged circulating time, low acute toxicity, and in addition to CT contrast, offered optical up-conversion luminescence (near infra-red (NIR) to visible or NIR to NIR). To extend its multimodal functionality, they included gadolinium for magnetic resonance imaging (MRI) as well as to contribute to the overall the X-ray attenuation. The initial basic particle, NaYbF4:Er, stabilized with oleic acid was noted to have considerable size and shape variation. Particle size and shape control was conveniently resolved through Gd-doping at 20+ mol%. Nevertheless, particle sizes ranged from 20 to 50 nm as determined by TEM. The particles provided marked CT contrast and were cleared into the liver and spleen. For MRI, the r1 relaxivity attributable to the gadolinium was 0.41 mM^{-1} s^{-1}, approximately a log$_{10}$ order below a typical MR blood pool contrast agent, e.g., Gd-DTPA, being ~4.5 mM^{-1} s^{-1}.

Pursuing a "soft" nanoparticle approach, Pan et al. [57] developed an ytterbium nanocolloid wherein a trivalent ytterbium complex suspended in polysorbate was encapsulated within a phospholipid membrane through microfluidization. The overall particle size was 240 nm with low polydispersity (0.2), a slightly negative zeta potential (−12 mV) and was designed for vascular constrained application, such as detection of ruptured plaque. The 20 % (v/v) nanocolloid suspension (~10^{12} particles/ml) contained 0.41 mg/ml of metallic Yb, which equated to approximately 1200 K Yb atoms/nanoparticle and was stable at 4 °C for months. Spectral CT imaging of the Yb^{3+} nanocolloid in the blood pool was clearly shown in the heart, perhaps the first K-edge image of Yb^{3+} produced (Fig. 6). However, largish nanoparticles provide considerably less blood pool contrast than small molecules or tiny particle on an equimolar basis, which is an advantage for vascular-targeted molecular imaging. The particles followed a typical biexponential pharmacokinetic profile with a beta-elimination $t_{1/2}$ of 5 h. Biodistribution of the nanocolloid was primarily in the liver and spleen acutely and whole body bioelimination was progressive over 1-week, with about 90 % elimination of the injected dose at 7 days. Similar to the bismuth neodecanoate nanocolloids, the Yb-based formulation could be further developed for detection of microthrombus in ruptured plaques or other vascular molecular imaging applications. However, in contradistinction to bismuth, which has a high K-edge (89.5 keV), the Yb^{3+}-based nanocolloid K-edge benefits in terms of contrast sensitivity and radiation dose from being more central within the photon energy spectrum of the X-ray beam.
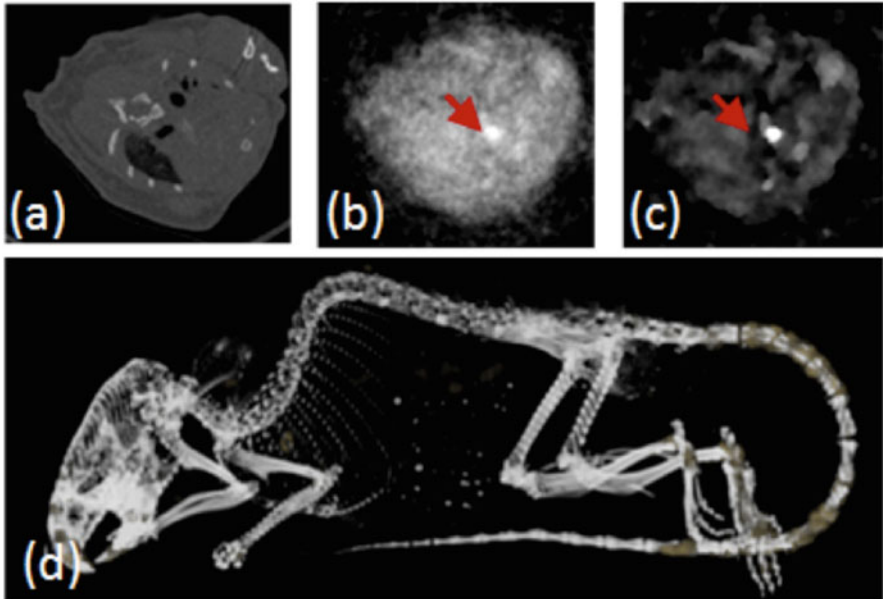
Fig. 6 Blood pool imaging in mouse after bolus injection of non-targeted Yb (2.46 mg/kg as a 20 vol% nanocolloid). The upper row shows a representative cross section through the heart. While change in contrast is only subtle in the conventional CT image (**a**), K-edge imaging using spectral CT and iterative reconstruction yields selective Yb signal at high signal to noise ratio (**b**, **c**, *red arrow*). The conventional CT and Yb images were used to compose a gradient rendered 3D image of the mouse (**d**) Reproduced with permission from Ref. [57]

8 Conclusions

Beyond iodinated systems, the recent increase in the development of CT contrast agents has coincided with the development of spectral CT. While these agents could all be envisioned for use with current clinical and dual energy CT, the incremental improvement over approved iodinated contrast agents, particularly for blood pool imaging, may be an economic barrier to translation. However, recent advancements in photon-counting detectors now place spectral CT clearly on the path to the clinic, offering higher resolution with lower radiation exposure as basic advantages. Spectral CT molecular imaging could be the "icing on the cake" that drives expansion of this capability by addressing intractable medical imaging issues unresolved today, such as the issue of coronary ruptured plaque in patients with possible ACS.

References

1. Alvarez RE, Macovski A. Energy-selective reconstructions in X-ray computerized tomography. Phys Med Biol. 1976;21(5):733–44.
2. Kelcz F, Joseph PM, Hilal SK. Noise considerations in dual energy CT scanning. Med Phys. 1979;6(5):418–25.

3. Lehmann LA, Alvarez RE, Macovski A, Brody WR, Pelc NJ, Riederer SJ, et al. Generalized image combinations in dual KVP digital radiography. Med Phys. 1981;8(5):659–67.

4. Brody WR, Cassel DM, Sommer FG, Lehmann LA, Macovski A, Alvarez RE, et al. Dual-energy projection radiography: initial clinical experience. AJR Am J Roentgenol. 1981;137(2):201–5.

5. Asaga T, Chiyasu S, Mastuda S, Mastuura H, Kato H, Ishida M, et al. Breast imaging: dual-energy projection radiography with digital radiography. Radiology. 1987;164(3):869–70.

6. Brooks RA, Di Chiro G. Split-detector computed tomography: a preliminary report. Radiology. 1978;126(1):255–7.

7. Barnes GT, Sones RA, Tesic MM, Morgan DR, Sanders JN. Detector for dual-energy digital radiography. Radiology. 1985;156(2):537–40.

8. Sones RA, Barnes GT. Noise correlations in images acquired simultaneously with a dual-energy sandwich detector. Med Phys. 1989;16(6):858–61.

9. Gauntt DM, Barnes GT. X-ray tube potential, filtration, and detector considerations in dual-energy chest radiography. Med Phys. 1994;21(2):203–18.

10. Alvarez RE. Active energy selective image detector for dual-energy computed radiography. Med Phys. 1996;23(10):1739–48.

11. Stevens GM, Pelc NJ. Depth-segmented detector for X-ray absorptiometry. Med Phys. 2000;27(5):1174–84.

12. Alvarez RE, Seibert JA, Thompson SK. Comparison of dual energy detector system performance. Med Phys. 2004;31(3):556–65.

13. Campbell M, Heijne EHM, Meddeler G, Pernigotti E, Snoeys W. A readout chip for a 64×64 pixel matrix with 15-bit single photon counting. IEEE Trans Nucl Sci. 1998;45(3):751–3.

14. Fischer P, Helmich A, Lindner M, Wermes N, Blanquart L. A photon counting pixel chip with energy windowing. IEEE Trans Nucl Sci. 2000;47(3):881–4.

15. Llopart X, Campbell M, Dinapoli R, Segundo DS, Pemigotti E. Medipix2: a 64-k pixel readout chip with 55 mu m square elements working in single photon counting mode. IEEE Trans Nucl Sci. 2002;49(5):2279–83.

16. Bronnimann C, Baur R, Eikenberry EF, Fischer P, Florin S, Horisberger R, et al. A pixel detector for the protein crystallography beamline at the SLS. Nucl Instrum Meth A. 2002;477(1–3): 531–5.

17. Locker M, Fischer P, Krimmel S, Kruger H, Lindner M, Nakazawa K, et al. Single photon counting X-ray imaging with Si and CdTe single chip pixel detectors and multichip pixel modules. IEEE Trans Nucl Sci. 2004;51(4):1717–23.

18. Roessl E, Brendel B, Engel KJ, Schlomka JP, Thran A, Proksa R. Sensitivity of photon-counting based K-edge imaging in X-ray computed tomography. IEEE Trans Med Imaging. 2011;30(9):1678–90.

19. Schirra CO, Brendel B, Anastasio MA, Roessl E. Spectral CT: a technology primer for contrast agent development. Contrast Media Mol Imaging. 2014;9(1):62–70.

20. Soo Choi H, Liu W, Misra P, Tanaka E, Zimmer JP, Itty Ipe B, et al. Renal clearance of quantum dots. Nat Biotech. 2007;25(10):1165–70.

21. Khlebtsov N, Dykman L. Biodistribution and toxicity of engineered gold nanoparticles: a review of in vitro and in vivo studies. Chem Soc Rev. 2011;40(3):1647–71.

22. Bulte JWM, Schmieder AH, Keupp J, Caruthers SD, Wickline SA, Lanza GM. MR cholangiography demonstrates unsuspected rapid biliary clearance of nanoparticles in rodents: Implications for clinical translation. Nanomedicine. 2014;10(7):1385–8.

23. Hampton JC. An electron microscope study of the hepatic uptake and excretion of submicroscopic particles injected into the blood stream and into the bile duct. Acta Anat. 1958;32:262–91.

24. Cho EC, Kim C, Zhou F, Cobley CM, Song KH, Chen J, et al. Measuring the optical absorption cross sections of Au-Ag nanocages and Au nanorods by photoacoustic imaging. J Phys Chem C Nanomater Interfaces. 2009;113(21):9023–8.

25. Park K, Park EJ, Chun IK, Choi K, Lee SH, Yoon J, et al. Bioavailability and toxicokinetics of citrate-coated silver nanoparticles in rats. Arch Pharm Res. 2011;34(1):153–8.

26. Skajaa T, Cormode DP, Jarzyna PA, Delshad A, Blachford C, Barazza A, et al. The biological properties of iron oxide core high-density lipoprotein in experimental atherosclerosis. Biomaterials. 2011;32(1):206–13.
27. Juhlin L. Excretion of intravenously injected solid particles in bile. Acta Physiol Scand. 1960;49:224–30.
28. Amsterdam EA, Kirk JD, Bluemke DA, Diercks D, Farkouh ME, Garvey JL, et al. Testing of low-risk patients presenting to the emergency department with chest pain. A scientific statement from the American Heart Association. Circulation. 2010;122:756–76.
29. Miller JM, Rochitte CE, Dewey M, Arbab-Zadeh A, Niinuma H, Gottlieb I, et al. Diagnostic performance of coronary angiography by 64-row CT. N Engl J Med. 2008;359(22):2324–36.
30. Arbab-Zadeh A, Miller JM, Rochitte CE, Dewey M, Niinuma H, Gottlieb I, et al. Diagnostic accuracy of computed tomography coronary angiography according to pre-test probability of coronary artery disease and severity of coronary arterial calcification: the CORE-64 (Coronary Artery Evaluation Using 64-Row Multidetector Computed Tomography Angiography) International Multicenter Study. J Am Coll Cardiol. 2012;59(4):379–87.
31. Pan D, Roessl E, Schlomka JP, Caruthers SD, Senpan A, Scott MJ, et al. Computed tomography in color: NanoK-enhanced spectral CT molecular imaging. Angew Chem Int Ed Engl. 2010;49(50):9635–9.
32. Barnett BP, Kraitchman DL, Lauzon C, Magee CA, Walczak P, Gilson WD, et al. Radiopaque alginate microcapsules for X-ray visualization and immunoprotection of cellular therapeutics. Mol Pharm. 2006;3(5):531–8.
33. Ai K, Liu Y, Liu J, Yuan Q, He Y, Lu L. Large-scale synthesis of Bi(2)S(3) nanodots as a contrast agent for in vivo X-ray computed tomography imaging. Adv Mater. 2011;23(42):4886–91.
34. Rabin O, Manuel Perez J, Grimm J, Wojtkiewicz G, Weissleder R. An X-ray computed tomography imaging agent based on long-circulating bismuth sulphide nanoparticles. Nat Mater. 2006;5(2):118–22.
35. Fang Y, Peng C, Guo R, Zheng L, Qin J, Zhou B, et al. Dendrimer-stabilized bismuth sulfide nanoparticles: synthesis, characterization, and potential computed tomography imaging applications. Analyst. 2013;138(11):3172–80.
36. Pan D, Pramanik M, Senpan A, Yang X, Song KH, Scott MJ, et al. Molecular photoacoustic tomography with colloidal nanobeacons. Angew Chem Int Ed Engl. 2009;48(23):4170–3.
37. Pan D, Pramanik M, Senpan A, Ghosh S, Wickline SA, Wang LV, et al. Near infrared photoacoustic detection of sentinel lymph nodes with gold nanobeacons. Biomaterials. 2010;31(14): 4088–93.
38. Pan D, Pramanik M, Senpan A, Allen JS, Zhang H, Wickline SA, et al. Molecular photoacoustic imaging of angiogenesis with integrin-targeted gold nanobeacons. FASEB J. 2011;25(3):875–82.
39. Schirra CO, Senpan A, Roessl E, Thran A, Stacy AJ, Wu L, et al. Second generation gold nanobeacons for robust K-edge imaging with multi-energy CT. J Mater Chem. 2012;22(43):23071–7.
40. Benson R. Present status of coronary artery disease. Arch Pathol Lab Med. 1926;2:876–916.
41. Constantinides P. Plaque fissuring in human coronary thrombosis. J Atheroscler Res. 1966;6:1–17.
42. Brown BG, Gallery CA, Badger RS, Kennedy JW, Mathey D, Bolson EL, et al. Incomplete lysis of thrombus in the moderate underlying atherosclerotic lesion during intracoronary infusion of streptokinase for acute myocardial infarction: quantitative angiographic observations. Circulation. 1986;73(4):653–61.
43. Fuster V, Badimon L, Cohen M, Ambrose JA, Badimon JJ, Chesebro J. Insight into the pathogenesis of acute ischemic syndromes. Circulation. 1988;77:1213–20.
44. Sanidas EA, Mintz GS, Maehara A, Cristea E, Wennerblom B, Iniguez A, et al. Adverse cardiovascular events arising from atherosclerotic lesions with and without angiographic disease progression. JACC Cardiovasc Imaging. 2012;5(3 Suppl):S95–105.
45. Cormode DP, Skajaa T, van Schooneveld MM, Koole R, Jarzyna P, Lobatto ME, et al. Nanocrystal core high-density lipoproteins: a multimodality contrast agent platform. Nano Lett. 2008;8(11):3715–23.

46. Cormode DP, Roessl E, Thran A, Skajaa T, Gordon RE, Schlomka J-P, et al. Atherosclerotic plaque composition: analysis with multicolor CT and targeted gold nanoparticles. Radiology. 2010;256:774–82.
47. Bulte JW. Science to practice: can CT be performed for multicolor molecular imaging? Radiology. 2010;256(3):675–6.
48. Peng C, Zheng L, Chen Q, Shen M, Guo R, Wang H, et al. PEGylated dendrimer-entrapped gold nanoparticles for in vivo blood pool and tumor imaging by computed tomography. Biomaterials. 2012;33(4):1107–19.
49. Zhu J, Fu F, Xiong Z, Shen M, Shi X. Dendrimer-entrapped gold nanoparticles modified with RGD peptide and alpha-tocopheryl succinate enable targeted theranostics of cancer cells. Colloids Surf B: Biointerfaces. 2015;133:36–42.
50. Al Zaki A, Joh D, Cheng Z, De Barros AL, Kao G, Dorsey J, et al. Gold-loaded polymeric micelles for computed tomography-guided radiation therapy treatment and radiosensitization. ACS Nano. 2014;8(1):104–12.
51. Douglass M, Bezak E, Penfold S. Monte Carlo investigation of the increased radiation deposition due to gold nanoparticles using kilovoltage and megavoltage photons in a 3D randomized cell model. Med Phys. 2013;40(7):071710.
52. Hainfeld JF, Dilmanian FA, Zhong Z, Slatkin DN, Kalef-Ezra JA, Smilowitz HM. Gold nanoparticles enhance the radiation therapy of a murine squamous cell carcinoma. Phys Med Biol. 2010;55(11):3045–59.
53. Chithrani DB, Jelveh S, Jalali F, van Prooijen M, Allen C, Bristow RG, et al. Gold nanoparticles as radiation sensitizers in cancer therapy. Radiat Res. 2010;173(6):719–28.
54. Bonitatibus Jr PJ, Torres AS, Goddard GD, FitzGerald PF, Kulkarni AM. Synthesis, characterization, and computed tomography imaging of a tantalum oxide nanoparticle imaging agent. Chem Commun (Camb). 2010;46(47):8956–8.
55. Oh MH, Lee N, Kim H, Park SP, Piao Y, Lee J, et al. Large-scale synthesis of bioinert tantalum oxide nanoparticles for X-ray computed tomography imaging and bimodal image-guided sentinel lymph node mapping. J Am Chem Soc. 2011;133(14):5508–15.
56. Liu Y, Ai K, Liu J, Yuan Q, He Y, Lu L. A high-performance ytterbium-based nanoparticulate contrast agent for in vivo X-ray computed tomography imaging. Angew Chem Int Ed Engl. 2012;51(6):1437–42.
57. Pan D, Schirra CO, Senpan A, Schmieder AH, Stacy AJ, Roessl E, et al. An early investigation of ytterbium nanocolloids for selective and quantitative "multicolor" spectral CT imaging. ACS Nano. 2012;6(4):3364–70.